Comparative compressional behavior of chabazite with Li^+, Na^+, Ag^+, K^+, Rb^+, and Cs^+ as extra-framework cations

by

Mihye Kong, Yongmoon Lee, G. Diego Gatta, Yongjae Lee

Corresponding author: **Yongjae Lee**, Department of Earth System sciences, Yonsei University, Seoul 03722, Republic of Korea - E-Mail: yongjaelee@yonsei.ac.kr

Manuscript submitted to The American Mineralogist for the special collection: "Microporous materials: crystal-chemistry, properties and utilizations"

Comparative compressional behavior of chabazite with Li^+, Na^+, Ag^+, K^+, Rb^+, and Cs^+ as extra-framework cations

Mihye Kong[1], Yongmoon Lee[2], G. Diego Gatta[3], Yongjae Lee[1, 2, *]

[1]Department of Earth System sciences, Yonsei University, Seoul 03722, Republic of Korea

[2]Center for High Pressure Science and Technology Advanced Research, Shanghai 201203, China

[3]Dipartimento di Scienze della Terra, Università degli Studi di Milano, Via Botticelli 23, I-20133 Milano, Italy

Abstract

The high-pressure behavior of monovalent-cation-exchanged chabazites was investigated by means of *in-situ* synchrotron X-ray powder diffraction with a diamond anvil cell, and using water as penetrating pressure-transmitting medium, up to 5.5 GPa at room temperature. In all cases, except for Na-containing chabazites, a phase transition from the original rhombohedral ($R\bar{3}m$) to triclinic symmetry (likely $P\bar{1}$) was observed in the range between 3.0 GPa and 5.0 GPa. The phase transition is accompanied by an abrupt decrease of the unit-cell volume by up to 10 %. Evidence of pressure-induced hydration (PIH), i.e., *P*-induced penetration of H_2O molecules through the zeolitic cavities, was observed, as reflected by the incompressibility of the cation-exchanged chabazites, which is governed by the distribution of the extra-framework cations. The reversibility of the PIH and *P*-induced phase transitions in the high-pressure behavior of the cation-exchanged chabazites are discussed in the context of the role played by the chemical nature and bonding configuration

of the extra-framework cations, along with that of the H_2O content at room conditions.

Keywords: Chabazite, compressibility, high pressure, pressure-induced hydration, synchrotron diffraction

Introduction

There is a growing interest in understanding the behavior of microporous materials at non-ambient conditions and, in particular, at high pressure (*e.g.*, Bish and Carey 2001; Alberti and Martucci 2005; Cruciani 2006; Gatta and Lee 2014; Gatta et al. 2017 and references therein). Pressure can cause important structural changes in microporous materials, modifying their physical-chemical properties and hence affecting their potential technological utilizations. Pressure-induced hydration (PIH) or pressure-induced insertion (PII), i.e., *P*-induced penetration of external molecules through the zeolitic sub-nanocavities at moderate pressure (≤ 1 GPa), is one of the most fascinating discovery in material science over the last decade, with potential technological and geological implications, recently reviewed by Gatta et al. (2017), promoting new routes for creating hybrid host-guest composite materials or for understanding the stability of clathrates or the role played by zeolites as carrier of H_2O or CO_2 in subduction zones (*e.g.*, Lee et al. 2011; Seoung et al. 2013; Seoung et al. 2014; Seoung et al. 2015; Im et al. 2015). Framework topology and extra-framework content are the key factors that govern the structural deformations at high pressure (*e.g.*, Gatta et al. 2005; Gatta 2010; Danisi et al. 2015). Previous studies showed that the pressure-induced deformation of the tetrahedral framework in zeolites can be described in terms of tilting of quasi-rigid tetrahedra (*e.g.*, Gatta 2008; 2010; Gatta and Lee 2014). There has not, however, been any systematic study on how the framework distortion in response to the applied pressure is influenced by the nature and distribution of the extra-framework cations. Only the "fibrous zeolites group", which was extensively investigated at high pressure, provided a preliminary model to describe the effect of the extra-framework population on the elastic behavior of isotypic materials (*e.g.*, Gatta 2005; Gatta et al. 2005; Seoung et al. 2013; Seoung et al. 2015).

Chabazite (ideally $|(Ca_{0.5},K,Na)_x(H_2O)_{12}|[Al_xSi_{12-x}O_{24}]$, with x = 2.4 - 5.0, http://www.iza-online.org/natural/Datasheets/Chabazite/chabazite.htm) is one of the most widespread natural zeolites with excellent ion-exchange properties (*e.g.*, Barrer et al. 1969;

Shang et al. 2012). Its framework is built up by double 6-membered rings (D6R), stacked in an ABC sequence and linked together through single 4-membered rings (S4R) (*e.g.,* Calligaris et al. 1982; Zema et al. 2008). As a result, the framework contains large ellipsoidal cavities (*i.e*., the CHA cage) with apertures of about 6.7 × 10 Å, which are accessible through single 8-rings (S8R) (Breck 1974). The largest opening of the S8R has a dimension of 3.8 × 3.8 Å and is located in the direction normal to the (001) crystal plane (Smith et al. 2001; Shang et al. 2012). Chabazites crystallizes with rhombohedral symmetry (space group $R\bar{3}m$), with only one independent tetrahedral framework site, populated by Al and Si with a statistically disordered distribution (Dent and Smith 1958). Exchangeable extra-framework cations and H_2O molecules are distributed over the D6R, S8R, and CHA cages with various occupancies (*e.g*., Fialips et al. 2005). A recent structural study of our group on various monovalent cation-exchanged chabazites revealed the systematic interplay between the framework and the extra-framework cations, *i.e.*, the unit-cell volume of monovalent-cation-exchanged chabazites varies in response to the ion selectivity, in the order of $Cs^+ \geq K^+ > Ag^+ > Rb^+ > Na^+ > Li^+$ (Kong et al. 2016).

The aim of this study is the description of the comparative compressional behavior of these monovalent cation-exchanged chabazites (Kong et al. 2016) and the potential crystal-fluid interactions in response to the applied hydrostatic pressure. We have performed *in-situ* high-pressure (at room temperature) synchrotron X-ray powder diffraction experiments on Li-, Na-, Ag-, K-, Rb-, and Cs-exchanged chabazites, using a diamond-anvil cell and pure water as a nominally pore-penetrating pressure-transmitting medium, in order to emulate the same conditions generated in industrial processes, or occurring in nature, in which water is the dominant *P*-fluid.

Experimental methods

A natural chabazite (hereafter ORI-CHA, $Ca_{1.6}Na_{0.5}Si_{8.4}Al_{3.6}O_{24}{\cdot}14.3H_2O$, space

group $R\bar{3}m$, a = 9.405(5) Å, α = 94.22(2)°) from Rubendorfel, Bohemia, was used in this study. Cation exchange was performed by stirring a mixture of ground ORI-CHA and the respective nitrate solution of Li, Na, Ag, K, Rb, and Cs, in a 1:100 weight ratio, in a closed system at 80°C for 72h. The final product was filtered, washed with distilled water, and air-dried. Elemental analysis (by X-ray fluorescence with energy-dispersive system detector) revealed that a complete ion-exchange was achieved, with the respective aforementioned cations. Further details pertaining to the ion-exchange protocols and cristallochemical characterization of the natural and final products are reported by Kong et al. (2016).

In-situ high-pressure (H*P*) synchrotron X-ray powder diffraction experiments on the as-prepared cation-forms of chabazites were performed at beamline 10-2 at the Stanford Synchrotron Radiation Lightsource (SSRL) at the SLAC National Accelerator Laboratory. At the beamline 10-2, the synchrotron radiation from the wiggler insertion device impinges on a Si(111) crystal followed by two pinholes in order to generate an approximately 200 μm diameter beam of monochromatic X-rays with a wavelength of 0.61992(5) Å. A Pilatus 300K-w Si-diode CMOS detector, manufactured by DECTRIS, was used to collect the powder diffraction data. The detector, held at a distance of 1032(2) mm from the sample, was stepped to produce scattering angle coverage in 2θ up to ca. 40°. The position of the incident beam, sample to detector distance, and detector tilt were determined using LaB_6 (SRM 660) as a standard polycrystalline material.

A modified Merrill-Bassett diamond anvil cell (DAC), with two opposing diamonds supported by tungsten-carbide plates, was used for the high-pressure X-ray diffraction measurements. A stainless-steel foil of 250 μm thickness was pre-indented to a thickness of about 100 μm, and a 300 μm hole was obtained by electro-spark erosion. The powdered samples of Li-, Na-, Ag-, K-, Rb-, and Cs-exchanged chabazites were placed in the gasket hole together with a few ruby chips (~20 μm in diameter) for pressure measurements by the ruby-fluorescence method (following the protocol of Mao et al. 1986; error: ± 0.05 GPa). Ambient pressure data were collected first on the dry zeolite powder sample inside the DAC.

Subsequently, pure water was added into the gasket hole as a (hydrostatic, at $P \leq 1$ GPa) *P*-transmitting medium (PTM), and the second ambient pressure data were collected using the 'wet' sample. The pressure was then increased and, at any pressure point, the sample was equilibrated for about 10 minutes before collecting the X-ray diffraction data. Water transforms to a solid phase at $P \geq 1$ GPa (and room temperature), and the diffraction peaks of ice VI and VII were observed at pressure in excess of 1 GPa. The experiments were deliberately performed under non-hydrostatic conditions at $P > 1$ GPa, in order to emulate the conditions of natural or industrial processes.

Pressure-dependent changes of the unit-cell lengths and volumes were derived from a series of Le Bail profile fittings (Le Bail et al. 1988) using the GSAS-EXPGUI suite of programs (Larson and Von Dreele 2004; Toby 2001). The background was fitted with a Chebyshev polynomial (with ≤ 24 coefficients), and the pseudo-Voigt profile function of Thompson et al. (1987) was used to model the Bragg peaks shape. Unfortunately, any attempt to perform Rietveld structure refinements (Rietveld 1969) was unsuccessful.

The (isothermal) bulk compressibility of the (low-*P*) rhombohedral polymorphs of Li^+-, Na^+-, Ag^+-, K^+-, Rb^+- and Cs^+-chabazites is here described by the bulk modulus K_0 ($K_0 = 1/\beta = -V \cdot \partial P/\partial V$, where β is the isothermal compressibility coefficient), obtained by a second-order Birch-Murnaghan Equation of State (II-BM-EoS) fit (Birch 1947), using the EOS-fit V7.0 program (Angel et al. 2014) and the data weighted by the uncertainties in *P* and *V*.

Results

Synchrotron X-ray powder diffraction patterns collected at high pressure, using pure water as PTM, are shown in Fig. 1. A visual examination of the diffraction patterns reveals that, upon increasing pressure, the diffraction peaks exhibit gradual broadening. The broadening effect can be due to a number of factors, such as an increase in the long-range structural disorder and the growth of microstrains in response to the non-hydrostatic

conditions at $P > 1$ GPa (*e.g.*, Yamanaka et al. 1997; Weidner et al. 1998; Fei and Wang 2000). Similar effects have been observed for the other isotypic CHA materials (*i.e.*, SAPO-34, ALPO-34) by Leardini et al. (2010, 2013). After pressure release back to ambient conditions, the peak positions, widths, and intensities revert back to those before compression, indicating the reversibility of the *P*-induced deformation mechanisms in all the cation-exchanged chabazites within the *P*-range investigated (Fig. 1). At $P > 3$ GPa, phase transitions from rhombohedral to triclinic symmetry are observed in chabazites exchanged with Li^+, K^+, Ag^+, Rb^+ and Cs^+, whereas the natural chabazite and the Na-form do not experience any transition (Figs. 1 and 2 and Table 1). These phase transitions are driven by an abrupt decrease of the unit-cell volume in the range between 2.0 and 10 % (Fig. 2).

The compressional pattern of the natural chabazite (ORI-CHA, $Ca_{1.6}Na_{0.5}Si_{8.4}Al_{3.6}O_{24}{\cdot}14.3H_2O$) in water PTM shows a monotonic trend, though with a softening which is more pronounced at $P > 2$ GPa (Figs. 1 and 2, Table 1). The refined bulk modulus (deduced on the basis of the low-*P* data pre-softening) is K_0 (ORI-CHA) = 88(3) GPa, while the measured unit-cell volume at ambient pressure is V_0 (ORI-CHA) = 824.9(9) $Å^3$.

When Li-CHA ($Li_{2.9}Si_{8.6}Al_{3.4}O_{24}{\cdot}13.2H_2O$) is compressed in water PTM from P_{amb} to 5.5 GPa, the unit-cell volume decreases steadily below 3.0 GPa. Above this pressure, the rhombohedral structure transforms into a triclinic one (Figs. 1 and 2, Table 1), accompanied by abrupt and anisotropic contraction of the unit-cell edges by ca. 0.8 %, 2.0 %, and 4.5 % for the *a*-, *b*-, and *c*-edge lengths, respectively, of the high-*P* triclinic polymorph (Fig. 2). This leads to an overall volume reduction by ca. 3.0 %. Bulk modulus at ambient pressure, calculated for the low-*P* rhombohedral polymorph of Li-CHA, is K_0 (Li-CHA) = 202(2) GPa with the measured V_0 (Li-CHA) of 819.9(9) $Å^3$. The bulk modulus of Li-CHA is the highest amongst the studied cation-exchanged chabazites (hence with the lowest compressibility), whereas its volume at ambient pressure is the smallest.

In the case of Na-CHA ($Na_{3.4}Si_{8.6}Al_{3.4}O_{24}\cdot 11.4H_2O$), compression in water PTM up to 5.3 GPa leads to a steady decrease of unit-cell volume without phase transition, though with a modest volume expansion at very low-P (0.5 GPa, Table 1) and softening at $P > 2$ GPa (Figs. 1 and 2, Table 1). The refined bulk modulus at ambient pressure (deduced on the basis of the low-P data pre-softening) is K_0 (Na-CHA) = 114(9) GPa with the measured V_0 (Na-CHA) of 824.9(9) Å^3.

In Ag-CHA($Ag_{3.5}Si_{8.5}Al_{3.5}O_{24}\cdot 15.9H_2O$), the steady initial contraction of the unit-cell edges in water PTM is followed by a transition to a triclinic structure above ca. 5.7 GPa, accompanying abrupt and anisotropic contractions of the a-, b-, and c-edge lengths, of the triclinic polymorph, by ca. 0.4 %, 3.3 %, and 8.7 %, respectively (Figs. 1 and 2, Table 1). This leads to an overall volume reduction by ca. 10.0 %. The refined bulk modulus at ambient pressure, calculated for the low-P rhombohedral polymorph of Ag-CHA, is K_0 (Ag-CHA) = 116(2) GPa with the measured V_0 (Ag-CHA) of 829.2(2) Å^3.

Similar transition from rhombohedral to triclinic structure is observed in K-CHA ($K_{3.2}Si_{8.7}Al_{3.3}O_{24}\cdot 10.7H_2O$) compressed in water at ca. 5.1 GPa (Figs. 1 and 2, Table 1). Also in this case, the transition is accompanied by abrupt and anisotropic contraction of the unit-cell edges by ca. 1.5 %, 1.5 %, and 6.5 % for the a-, b-, and c-edge lengths, respectively (Fig. 2), which leads to an overall volume reduction of the high-P triclinic polymorph by ca. 6.0 %. The refined bulk modulus of the low-P rhombohedral polymorph of K-CHA is K_0 (K-CHA) = 93(1) GPa, the lowest value amongst the ion-exchanged chabazites of this study, whereas the measured unit-cell volume at ambient pressure is V_0 (K-CHA) = 830.8(8) Å^3.

Compression of Rb-CHA ($Rb_{4.1}Si_{7.9}Al_{4.1}O_{24}\cdot 6.5H_2O$) in water PTM to 6.0 GPa shows a modest volume expansion at very low-P (0.5 GPa, Table 1) and then a gradual monotonic decrease of the unit-cell volume up to ca. 4.9 GPa, followed by abrupt contraction by ca. 5.0 % in response to the rhombohedral-to-triclinic phase transition (Figs. 1 and 2, Table 1). This transition is also driven by anisotropic contraction of the unit-cell edges, of the triclinic

polymorph, by ca. 1.9 %, 0.7 %, and 4.8 % for the *a*-, *b*-, and *c*-edge lengths, respectively (Fig. 2). The refined bulk modulus of low-*P* rhombohedral Rb-CHA is the second largest after Li-CHA: K_0 (Rb-CHA) = 149(5) GPa, with a measured V_0 (Rb-CHA) = 826.0(1) Å^3.

For Cs-CHA ($Cs_{3.4}Si_{8.6}Al_{3.4}O_{24}\cdot 6.4H_2O$), a modest volume expansion at very low-*P* (0.5 GPa, Table 1) followed by a monotonic compression is also observed (Figs. 1 and 2, Table 1). The degree of volume contraction during the rhombohedral-to-triclinic transition, between 3 and 4 GPa, is modulated to ca. 2.0% with anisotropic reduction of the unit-cell edges by ca. 1.4 %, 1.2 %, and 1.1 % for the *a*-, *b*-, and *c*-edges lengths, respectively, of the triclinic form (Figs. 1 and 2, Table 1). Bulk modulus and (measured) unit-cell volume at ambient pressure for the low-*P* rhombohedral polymorph are: K_0 (Cs-CHA) = 137(1) GPa and V_0 (Cs-CHA) = 830.4(4) Å^3, respectively.

Discussion and Implications

The experimental findings of this study, in which a nominally penetrating *P*-transmitting fluid is used (*sensu* Gatta 2008), allow first of all a comparison between the compressional behavior of a natural chabazite in penetrating and non-penetrating media. Leardini et al. (2010, 2013) reported the behavior of two natural chabazites, with slightly different compositions, compressed in silicone oil (a non-penetrating *P*-medium) and showed: a change of the compressional behavior at 1.4 GPa in one of the samples, with chemical formula $(K_{1.36}Ca_{1.04}Na_{0.28}Sr_{0.4}Ba_{0.06}Mg_{0.02})[Si_{7.17}Al_{4.87}O_{24}]\cdot 13.16H_2O$, with an estimated bulk modulus of 35(5) GPa at $P < 1.4$ GPa and 62(1) at $P > 1.4$ GPa (Leardini et al. 2010); a rhombohedral-to-triclinic phase transition at 2.1 GPa in the second chabazite sample, with chemical formula $(Ca_{1.32}K_{0.45}Na_{0.13}Sr_{0.10})[Si_{8.55}Al_{3.45}O_{24}]\cdot 11.30H_2O$, with an estimated bulk modulus of 54(3) GPa for the low-*P* polymorph. Further H*P*-experiments on the synthetic ALPO-34 and SAPO-34, isotypic materials with CHA framework topology, were performed using non-penetrating fluids: the bulk modulus of the ALPO-34 was reported to be 54(3)

(Leardini et al. 2012) and that of SAPO-34 of 29(1) GPa (Leardini et al. 2010). ALPO-34 and SAPO-34 are materials with a nominally neutral framework, and thus with no extra-framework cations. If we consider all the data available in the open literature, the "expected" bulk modulus (at room conditions) of a natural (rhombohedral) chabazite is 50±15 GPa. In our study, the bulk modulus of the natural chabazite compressed in water, a nominally penetrating fluid, leads to a bulk modulus of about 90 GPa. This value is, in general, unusual for zeolites (*i.e.*, too high, Gatta and Lee 2014) and, in this specific case, suggests that the H_2O molecules penetrate through the zeolitic cavities in response to the applied pressure. The continuous penetration of the extra H_2O molecules would lead to more efficient stuffing of the pores by extra-framework species, making the zeolite structure less compressible. This can explain the higher bulk modulus observed in this study if compared to those obtained in previous experiments with non-penetrating *P*-fluids, in which the inherent compressibility is obtained. A similar effect was previously observed in several H*P*-experiments on zeolites (compressed in penetrating and non-penetrating fluids) and provides "indirect" evidence of PIH in our experiment, useful when "direct" evidence are missed due to the lack of abrupt structural changes and/or structural models (*i.e.*, impossibility to perform Rietveld structure refinements).

Without data at atomic scale obtained by structure refinements, it is not sure if the penetration of extra H_2O molecules occurs entirely at very low-*P* ($\leq$ 0.5 GPa), as suggested by the modest volume expansion in Na-, Rb- and Cs-CHA (Table 1) and as observed for several zeolites (Gatta 2008; Gatta and Lee 2014 and references therein), or it is a continuous process within the *P*-range investigated. In the second case, the bulk modulus value does not have a robust physical meaning, because the composition of the zeolite changes with increasing pressure (*i.e.*, the system is "open"). However, the "apparent" compressibility, through the bulk modulus, remains a useful measure for a comparative analysis (*e.g.*, the same zeolite compressed in different fluids; zeolites with the same framework topology and different extra-framework population compressed in the same fluid).

The compressional behavior of all the cation-exchanged chabazites of this study allow us to make the following observations and considerations:

1) Our results indicate an inverse relationship between the onset pressure of the rhombohedral-to-triclinic transition and the radius of extra-framework cation in chabazite, above the ca. 1.0 Å threshold (Fig. 3). Similar trend is observed between the degree of volume contraction and the radius of extra-framework cation, which appears to be mainly driven by the *c*-edge length contraction of the triclinic polymorph (Fig. 3, Table 1). The largest contraction along the *c*-axis is ca. 8.7% in Ag-CHA, whereas in K-CHA, Rb-CHA, and Cs-CHA, the contractions are by ca. 6.5, 4.8, and 1.4%, respectively (Fig. 3). The different volume contraction, in response to the phase transition, might be partly related to the initial H_2O content at ambient conditions. In Ag-CHA there are ca. 15.9 H_2O molecules per formula unit (p.f.u.), which decrease to ca. 10.7, 6.5, and 6.4 in K-CHA, Rb-CHA, and Cs-CHA, respectively (Fig. 3). On the other hand, there are ca. 13.2 H_2O p.f.u. in Li-CHA, which exhibits lower transition pressure and volume contraction than Ag-CHA (Fig. 3): Li-CHA appears to be an outlier in the contraction vs. cation radius relationship and needs further structural investigation.
2) There is an additional experimental finding about a potential relation between the observed bulk modulus and the distribution of extra-framework cations over the different segments forming the chabazite cavities, *i.e.*, D6R, S8R, and CHA-cage (Fig. 4). The highest bulk modulus of 202(2) GPa is observed for the rhombohedral low-*P* polymorph of Li-CHA, where Li-cations fill all the three cavities (D6R, S8R, and CHA-cage) at ambient conditions. More compressible than Li-CHA are Rb-CHA and Cs-CHA with bulk moduli of 149(5) and 137(1) GPa, respectively. In these chabazites, the extra-framework cations populate the S8R and CHA-cages only (*i.e.*, no D6R). The most compressible forms are then Ag-CHA, Na-CHA, and K-CHA with bulk moduli of 116(2), 114(9), and 93(1) GPa, respectively. In these compounds, extra-

framework cations are only located in the largest CHA-cages (*i.e.*, no D6R or S8R).

3) All the high-*P* deformation mechanisms and penetration phenomena are reversible, as proved by the diffraction data collected at room conditions after decompression (Fig. 1, Table 1).

Overall, it appears that:

1) PIH occurs in the natural and in all the cation-exchanged chabazites of this study, and it is reversible. This is true even in the case of Na-CHA, which does not experience any *P*-induced phase transition but reacts, in response to the applied pressure, with a bulk modulus of 114(9) GPa, not realistic for a zeolite without any crystal-fluid interaction (Gatta 2008, Gatta and Lee 2014). At this stage, it is unknown why the ORI-CHA and Na-CHA do not experience the *P*-induced phase transition observed for the other cation-exchanged forms of this study. Likely, the higher number of independent extra-framework sites in these two chabazites (*i.e.*, ORI-CHA: 4Ca + 3Na + 5OW; Na-CHA: 4Na + 7OW; Li-CHA: 4Li + 5OW; K-CHA: 3K + 5OW; Rb-CHA: 2Rb + 2OW; Cs-CHA: 2Cs + 2OW; Ag-CHA: 2Ag + 2OW; Kong et al. 2016) makes their structures more "flexible", with higher degrees of freedom accommodating the *P*-induced deformation effects.

2) The degree of PIH is someway controlled by the distribution of the extra-framework cations (which, in turn, reflects their ionic radius and charge) and how these can coordinate extra H_2O molecules. Li, for example, is a small ion and its coordination polyhedra leaves room in the cavities for additional H_2O molecules, which can be further coordinated by Li or can be H-bonded to the framework oxygens. However, the different number (and location inside the cavities) of independent cation sites and H_2O molecules in the cation-exchanged chabazites of this study does not allow to define a universal and unambiguous model to explain the behavior of all the cation-exchanged chabazites.

We can draw geological implications of our experimental findings as follows. Our results demonstrate that small molecules (in kinetic diameters), like H_2O, CO_2, CH_4 or H_2S, can potentially penetrate into the CHA-type zeolites in response to the applied pressure. Such a penetration phenomenon is likely to be active even at very low pressures (kilobar level or even lower). Geological fluids can, therefore, interact efficiently with this zeolite with a significant fluid-to-crystal mass transfer. In other words, the ability of zeolites, as microporous materials, to act as geochemical traps of small molecules can be drastically enhanced at moderate pressures even at room temperature; it is highly likely that the combined effect of pressure and temperature would improve the magnitude of the PIH and PII, as previously observed in other zeolites (Gatta and Lee 2014 and references therein).

The technological implications of our results are even more relevant. Our experimental findings demonstrate that it is possible to modulate the elastic behavior of a given zeolite simply by cation-exchange and using a penetrating *P*-transmitting fluid. A combined [A^+-CHA + H_2O] system (with A^+ = Li, Na, Ag, K, Rb, Cs) can behave like a low-compressibility "spring": the bulk modulus of the Li-CHA in H_2O (*i.e.*, 202(2) GPa) is higher, in certain *P*-range, than those of garnets (~190 GPa, Hazen et al. 1994), mullites (~ 170 GPa, Gatta et al. 2010, 2013) or topaz (~160 GPa, Gatta et al. 2006, 2014). With different cations, it is possible to generate hybrid softer systems with modulated bulk moduli targeting certain solids such as olivines (~ 120-130 GPa, Smyth et al. 2000), pyroxenes (~ 90-130 GPa, McCarthy et al. 2008) or feldspars (~ 50-80 GPa, Angel 2004). This is surprising if we consider that zeolites are microporous materials and intuitively considered as soft compounds. PIH observed in this study for the natural and for all the cation-exchanged chabazites, is a reversible phenomenon and cannot be used to generate super-hydrated zeolites which remain metastable at room conditions after decompression. However, it would be different for other small molecules and/or mixed cation chabazites. In this light, further studies are in progress in order to expand the number of small molecules able to penetrate the CHA-cavities at high pressure.

343

344

345 **Acknowledgments**

346 This work was supported by the Global Research Laboratory (NRF-2009-00408) and
347 National Research Laboratory (NRF-2015R1A2A1A01007227) programs of the Korean
348 Ministry of Science, ICT and Planning (MSIP). We also thank the supports by NRF-
349 2016K1A4A3914691 and NRF-2016K1A3A7A09005244 grants. Experiments using X-ray
350 synchrotron radiation were supported by the Collaborative Access Program of SSRL.

References

Alberti, A. and Martucci, A. (2005) Phase transformations and structural modifications induced by heating in microporous materials. Studies in surface science and catalysis, 155, 19-43.

Angel, R.J. (2004) Equations of state of plagioclase feldspars. Contributions to Mineralogy and Petrology, 146, 506–512.

Angel, R.J., Gonzalez-Platas, J., and Alvaro, M. (2014) EosFit-7c and a fortran module (library) for equation of state calculations. Zeitschrift für Kristallographie, 229, 405-419.

Barrer, R.M., Davies, J.A., and Rees, L.V.C. (1969) Thermodynamics and thermochemistry of cation exchange in chabazite. Journal of Nuclide Chemistry, 31, 219-232.

Bish, D.L. and Carey, J.W. (2001) Thermal behavior of natural zeolites. Reviews in Mineralogy and Geochemistry, 45, 403–452.

Birch, F. (1947) Finite elastic strain of cubic crystals. Physical Review, 71, 809-824.

Breck, D.W. (1974) Zeolite molecular sieves: Structure, chemistry and use. Wiley and Sons, New York (original edition); reprinted R.E. Kriegger, F.L. Malabar, 1984 (new edition).

Calligaris, M., Nardin, G., and Randaccio, L. (1982) Cation-site location in a natural chabazite. Acta Crystallographica, B38, 602-605.

Cruciani, G. (2006) Zeolites upon heating: Factors governing their thermal stability and structural changes. Journal of Physics and Chemistry of Solids, 67, 1913-2240.

Danisi, R.M., Armbruster, T., Arletti, R., Gatta, G.D., Vezzalini, G., Quartieri, S., and Dmitriev, V. (2015) Elastic behavior and pressure-induced structural modifications of the microporous $Ca(VO)Si_4O_{10}\cdot 4H_2O$ dimorphs cavansite and pentagonite. Microporous and

375 Mesoporous Materials, 204, 257-268.

376 Dent, L.S. and Smith, J.V. (1958) Crystal structure of chabazite, a molecular sieve.
377 Nature, 181, 1794-1796.

378 Fei, Y. and Wang, Y. (2000) High-pressure and high-temperature powder diffraction.
379 Reviews in Mineralogy and Geochemistry, 41, 521-557.

380 Fialips, C.I., Carey, J.W., and Bish, D.L. (2005) Hydration-dehydration behavior and
381 thermodynamics of chabazite. Geochimica et Cosmochimica Acta, 69, 2293-2308.

382 Gatta, G.D. (2005) A comparative study of fibrous zeolites under pressure. European
383 Journal of Mineralogy, 17, 411-421.

384 Gatta, G.D. (2008) Does porous mean soft? On the elastic behavior and structural
385 evolution of zeolites under pressure. Zeitschrift für Kristallographie, 223, 160-170.

386 Gatta, G.D. (2010) Extreme deformation mechanisms in open-framework silicates at
387 high-pressure: Evidence of anomalous inter-tetrahedral angles. Microporous and Mesoporous
388 Materials, 128, 78–84.

389 Gatta, G.D. and Lee, Y. (2014) Zeolites at high pressure: A review. Mineralogical
390 Magazine, 78, 267-291.

391 Gatta, G.D., Boffa Ballaran, T., Comodi, P., and Zanazzi, P.F. (2004) Comparative
392 compressibility and equation of state of orthorhombic and tetragonal edingtonite. Physics and
393 Chemistry of Minerals, 31, 288-298.

394 Gatta, G.D., Nestola, F., and Boffa Ballaran, T. (2006) Elastic behaviour and
395 structural evolution of topaz at high pressure. Physics and Chemistry of Minerals, 33, 235-
396 242.

397 Gatta, G.D., Rotiroti, N., Fisch, M., and Armbruster, T. (2010) Stability at high
398 pressure, elastic behavior and pressure-induced structural evolution of ‘‘Al_5BO_9’’, a mullite-

399 type ceramic material. Physics and Chemistry of Minerals, 37, 227-236.

400 Gatta, G.D., Lotti, P., Merlini, M., Liermann, H.-P., and Fisch, M. (2013) High-
401 pressure behavior and phase stability of Al_5BO_9, a mullite-type ceramic material. Journal of
402 the American Ceramic Society, 96, 2583–2592.

403 Gatta, G.D., Morgenroth, W., Dera, P., Petitgirard, S., and Liermann, H-P. (2014)
404 Elastic behavior and pressure-induced structure evolution of topaz up to 45 GPa. Physics and
405 Chemistry of Minerals, 41, 569-577.

406 Gatta, G.D., Lotti, P., and Tabacchi, G. (2017) The effect of pressure on open-
407 framework silicates: elastic behaviour and crystal–fluid interaction. Physics and Chemistry of
408 Minerals (in press, DOI: 10.1007/s00269-017-0916-z).

409 Hazen, R.M., Downs, R.T., Conrad, P.G., Finger, L.W., and Gasparik, T. (1994)
410 Comparative compressibilities of majorite-type garnets. Physics and Chemistry of Minerals,
411 21, 344–349.

412 Im, J., Seoung, D., Lee, S.Y., Blom, D.A., Vogt, T., Kao, C.-C., and Lee, Y. (2015)
413 Pressure-Induced Metathesis Reaction To Sequester Cs. Environmental Science and
414 Technology, 49, 513-519.

415 Kong, M., Liu, Z., Vogt, T., and Lee, Y. (2016) Chabazite structures with Li^+, Na^+,
416 Ag^+, K^+, NH_4^+, Rb^+ and Cs^+ as extra-framework cations. Microporous and Mesoporous
417 Materials, 221, 253-263.

418 Larson, A.C. and Von Dreele, R.B. (2004) General structure analysis system (GSAS),
419 Los Alamos National Laboratory Report LAUR 86–748.

420 Leardini, L., Quartieri, S., and Vezzalini, G. (2010) Compressibility of microporous
421 materials with CHA topology: 1. Natural chabazite and SAPO-34. Microporous and
422 Mesoporous Materials, 127, 219-227.

Leardini, L., Quartieri, S., Vezzalini, G., Martucci, A., and Dmitriev, V. (2013) Elastic behavior and high pressure-induced phase transition in chabazite: New data from a natural sample from Nova Scotia. Microporous and Mesoporous Materials, 170, 52-61.

Le Bail, A., Duroy, H., and Fourquet, J.L. (1988) Ab-initio structure determination of $LiSbWO_6$ by X-ray powder diffraction. Materials Research Bulletin, 23, 447–452.

Lee, Y., Liu, D., Seoung, D., Liu, Z., Kao, C.-C., and Vogt, T. (2011) Pressure- and Heat-Induced Insertion of CO_2 into an Auxetic Small-Pore Zeolite. Journal of the American Chemical Society, 133, 1674-1677.

Mao, H.K., Xu, J., and Bell, P.M. (1986) Calibration of the ruby pressure gauge to 800 kbar under quasi-hydrostatic conditions. Journal of Geophysical Research, 91, 4673–4676.

McCarthy, A.C., Downs, R.T., and Thompson, R.M. (2008) Compressibility trends of the clinopyroxenes, and in-situ high-pressure single-crystal X-ray diffraction study of jadeite. American Mineralogist, 93, 198–209.

Seoung, D., Lee, Y., Kao, C.-C., Vogt, T., and Lee, Y. (2013) Super-Hydrated Zeolites: Pressure-Induced Hydration in Natrolites. Chemistry - A European Journal, 19, 10876–10883.

Seoung, D., Lee, Y., Cynn, H., Park, C., Choi, K.-Y., Blom, D.A., Evans, W.J., Kao, C.-C., Vogt, T., and Lee, Y. (2014) Irreversible Xenon Insertion into a Small Pore Zeolite at Moderate Pressures and Temperatures. Nature Chemistry, 6, 835-839.

Seoung, D., Lee, Y. Kao, C.-C., Vogt, T., and Lee, Y. (2015) Two-Step Pressure-Induced Superhydration in Small Pore Natrolite with Divalent Extra-Framework Cations. Chemistry of Materials, 27, 3874-3880.

Shang, J., Li, G., Singh, R., Gu, Q., Nairn, K.M., Bastow, T.J., Medhekar, N., Doherty, C.M., Hill, A.J., Liu, J.Z., and Webley, P.A. (2012) Discriminative Separation of Gases by a “Molecular Trapdoor” Mechanism in Chabazite Zeolites. Journal of the American

448 Chemical Society, 134, 19246-19253.

449 Smith, L.J., Eckert, H., and Cheetham, A.K. (2001) Potassium cation effects on site
450 preferences in the mixed cation zeolite Li, Na-chabazite. Chemistry of Materials, 13, 385-391.

451 Smyth, J.R., Jacobsen, S.D., and Hazen, R.M. (2000) Comparative crystal chemistry
452 of orthosilicate minerals. Reviews in Mineralogy and Geochemistry, 41, 187-209.

453 Thompson, P., Cox, D.E., and Hastings, J.B. (1987) Rietveld refinement of Debye-
454 Scherrer synchrotron X-ray data from Al_2O_3. Journal of Applied Crystallography, 20, 79-83.

455 Toby, B.H. (2001) EXPGUI, a graphical user interface for GSAS. Journal of Applied
456 Crystallography, 34, 210-213.

457 Rietveld, H.M. (1969) A profile refinement method for nuclear and magnetic
458 structures. Journal of Applied Crystallography, 2, 65–71.

459 Weidner, D.J., Wang, Y.B., Chen, G., Ando, J., and Vaughan, M.T. (1998) Rheology
460 measurements at high pressure and temperature. In M.H. Manghnani and T. Yagi, Eds.,
461 Properties of Earth and Planetary Materials at High Pressure and Temperature. Geophysical
462 Monograph. American Geophysical Union, Washington, DC, p. 473–480.

463 Yamanaka, T., Nagai, T., and Tsuchiya, T. (1997) Mechanism of pressure-induced
464 amorphization. Zeitschrift für Kristallographie, 212, 401-410.

465 Zema, M., Tarantino, S.C., and Montagna, G. (2008) Hydration/Dehydration and
466 cation migration processes at high temperature in zeolite chabazite. Chemistry of Materials,
467 20, 5876-5887.

468

469

Figure captions

Figure 1. Synchrotron X-ray powder diffraction patterns as a function of hydrostatic pressure mediated by pure water as *P*-transmitting medium for (a) ORI-CHA, (b) Li-CHA, (c) Na-CHA, (d) Ag-CHA, (e) K-CHA, (f) Rb-CHA, and (g) Cs-CHA. Some of the new peak positions due to symmetry lowering are indicated with Miller indices.

Figure 2. Evolution of the unit-cell edges lengths (Å) and volume (Å^3) with *P*, using pure water as *P*-transmitting medium, for (a) ORI-CHA, (b) Li-CHA, (c) Na-CHA, (d) Ag-CHA, (e) K-CHA, (f) Rb-CHA, and (g) Cs-CHA. The errors associated with the cell parameters are smaller than the symbols. The dashed lines represent only a guide for eyes. For the unit-cell volume, the red symbols indicate the triclinic high-*P* polymorphs.

Figure 3. Changes in the (a) unit-cell volume, (b) *c*-edge length, and (c) onset pressure of the rhombohedral-to-triclinic transition as a function of the ionic radius of the extra-framework cation in the alkali-metal-exchanged chabazites.

Figure 4. (a) Site distribution and (b) occupancy of the extra-framework cations, and (c) initial H_2O molecular contents per formula unit in the alkali-metal-exchanged chabazites at ambient conditions. (d) "Observed" bulk moduli plotted as a function of cation radius.

Figure 1..

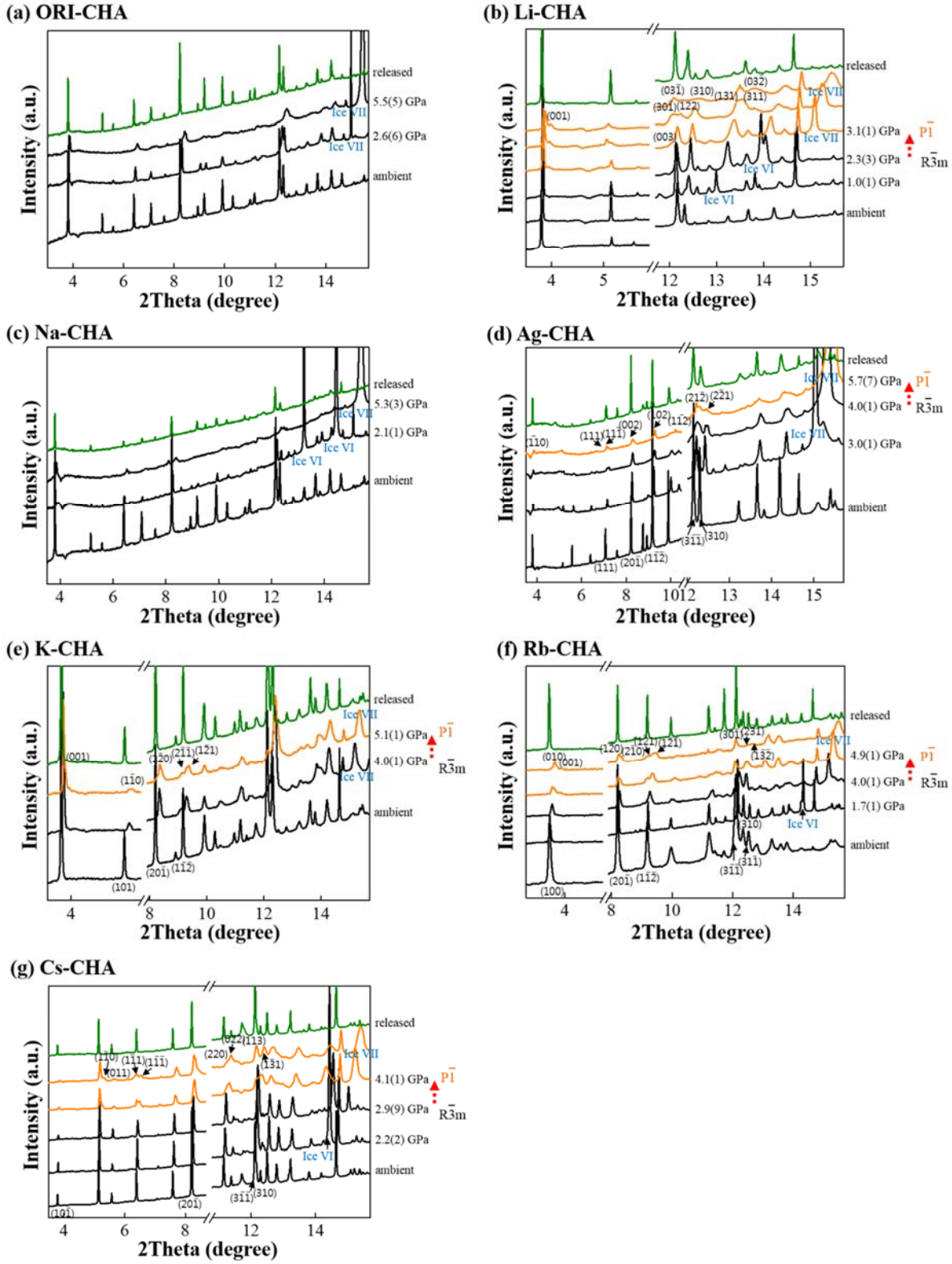
(a) ORI-CHA
Intensity (a.u.)
2Theta (degree)
released
5.5(5) GPa
2.6(6) GPa
ambient
Ice VII
(b) Li-CHA
3.1(1) GPa
2.3(3) GPa
1.0(1) GPa
Ice VI
(c) Na-CHA
5.3(3) GPa
2.1(1) GPa
(d) Ag-CHA
5.7(7) GPa
4.0(1) GPa
3.0(1) GPa
(e) K-CHA
5.1(1) GPa
(f) Rb-CHA
4.9(1) GPa
1.7(1) GPa
(g) Cs-CHA
4.1(1) GPa
2.9(9) GPa
2.2(2) GPa
P1̄
R3̄m

Figure 2.

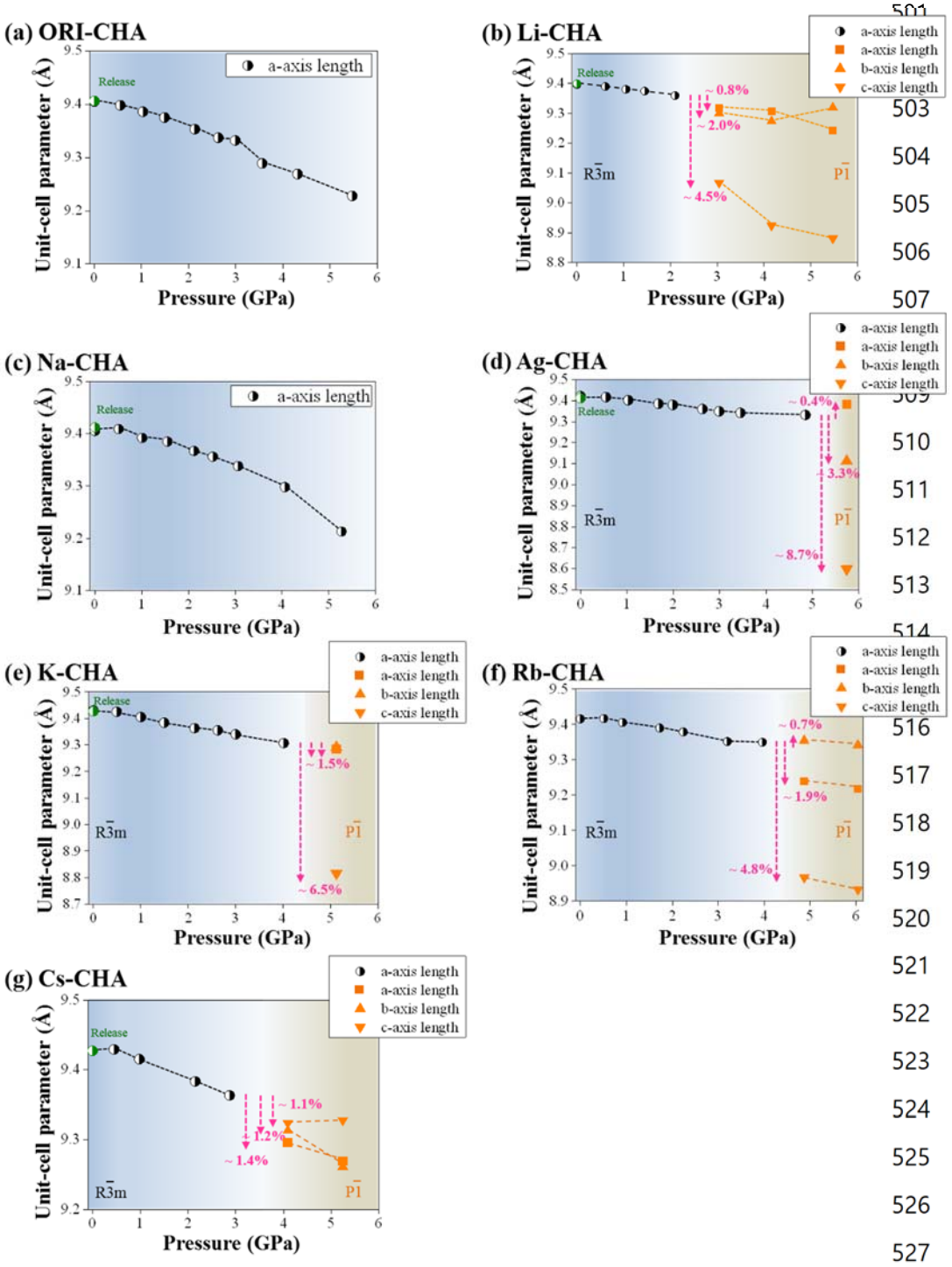
(a) ORI-CHA
a-axis length
Release
Unit-cell parameter (Å)
Pressure (GPa)
(b) Li-CHA
a-axis length
a-axis length
b-axis length
c-axis length
Release
~ 0.8%
~ 2.0%
~ 4.5%
R3̄m
P1̄
Unit-cell parameter (Å)
Pressure (GPa)
(c) Na-CHA
a-axis length
Release
Unit-cell parameter (Å)
Pressure (GPa)
(d) Ag-CHA
a-axis length
a-axis length
b-axis length
c-axis length
Release
~ 0.4%
~ 3.3%
~ 8.7%
R3̄m
P1̄
Unit-cell parameter (Å)
Pressure (GPa)
(e) K-CHA
a-axis length
a-axis length
b-axis length
c-axis length
Release
~ 1.5%
~ 6.5%
R3̄m
P1̄
Unit-cell parameter (Å)
Pressure (GPa)
(f) Rb-CHA
a-axis length
a-axis length
b-axis length
c-axis length
~ 0.7%
~ 1.9%
~ 4.8%
R3̄m
P1̄
Unit-cell parameter (Å)
Pressure (GPa)
(g) Cs-CHA
a-axis length
a-axis length
b-axis length
c-axis length
Release
~ 1.1%
~ 1.2%
~ 1.4%
R3̄m
P1̄
Unit-cell parameter (Å)
Pressure (GPa)

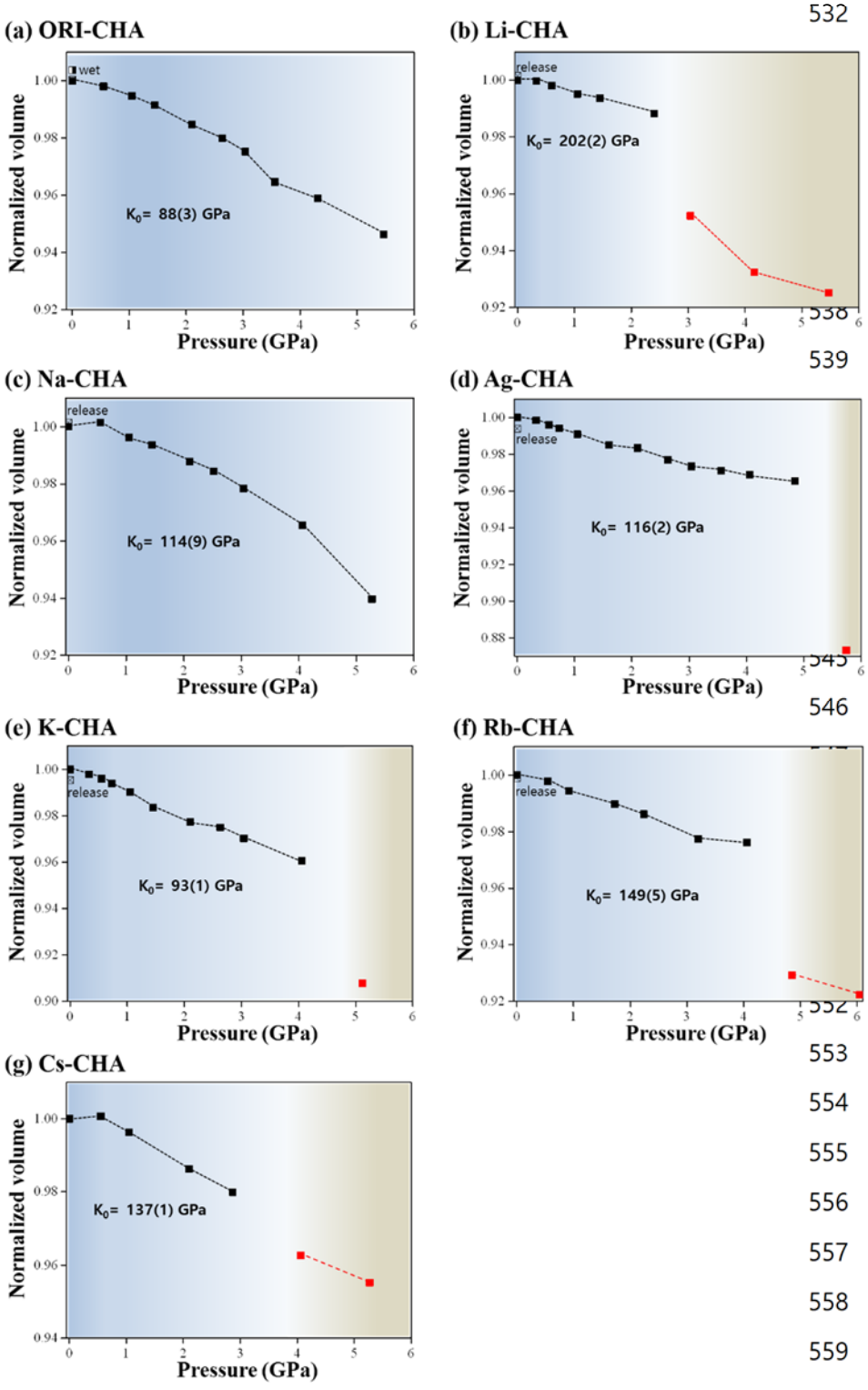
(a) ORI-CHA
wet
K_0= 88(3) GPa
(b) Li-CHA
release
K_0= 202(2) GPa
(c) Na-CHA
release
K_0= 114(9) GPa
(d) Ag-CHA
release
release
K_0= 116(2) GPa
(e) K-CHA
release
K_0= 93(1) GPa
(f) Rb-CHA
release
K_0= 149(5) GPa
(g) Cs-CHA
K_0= 137(1) GPa
Normalized volume
Pressure (GPa)

Figure 3.

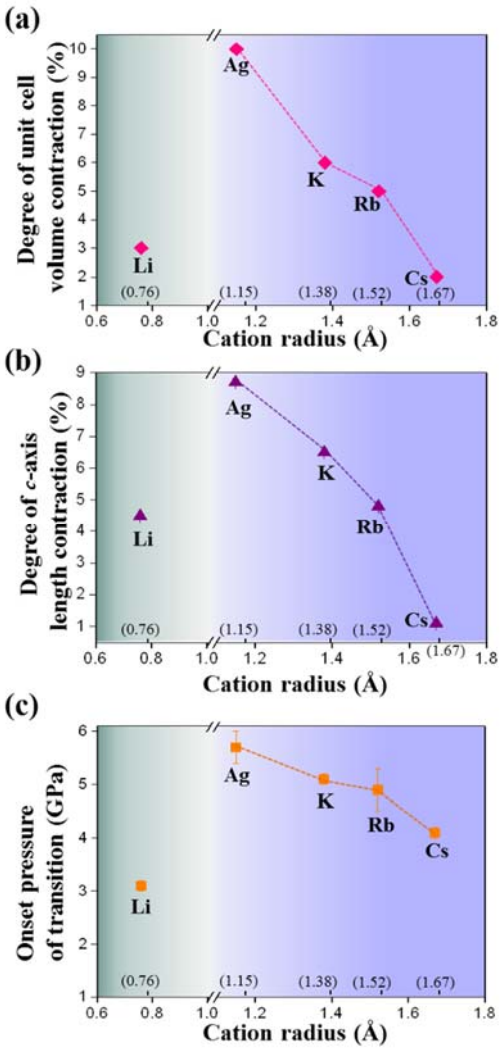
(a)
Degree of unit cell volume contraction (%)
Ag
K
Rb
Cs
Li
(0.76)
(1.15)
(1.38)
(1.52)
(1.67)
Cation radius (Å)
(b)
Degree of c-axis length contraction (%)
Ag
K
Rb
Cs
Li
(0.76)
(1.15)
(1.38)
(1.52)
(1.67)
Cation radius (Å)
(c)
Onset pressure of transition (GPa)
Ag
K
Rb
Cs
Li
(0.76)
(1.15)
(1.38)
(1.52)
(1.67)
Cation radius (Å)

591 Figure 4.

592

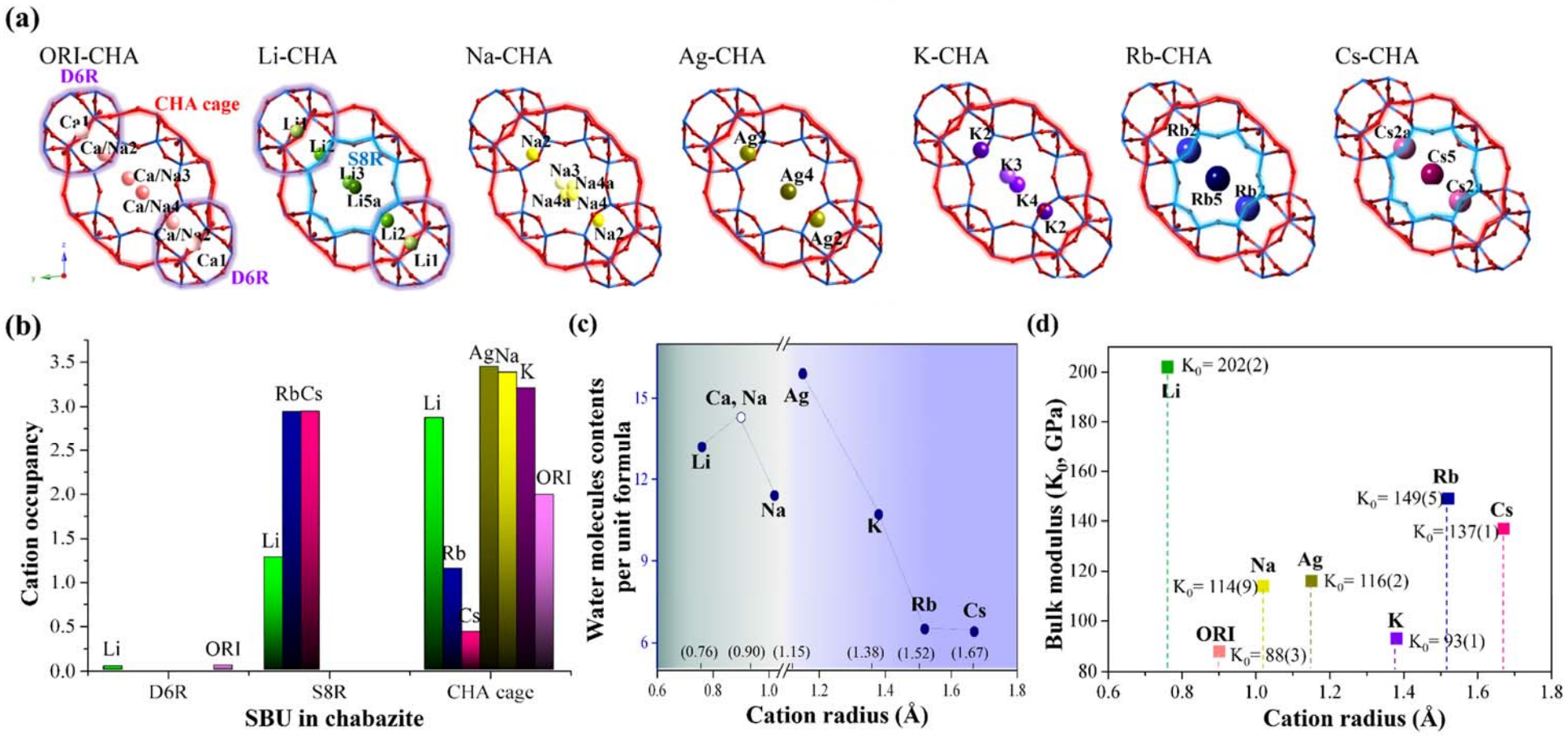

Table 1. Changes in the unit-cell edge lengths and volume of the cation-exchanged chabazites with *P*, compressed in pure water as pore-penetrating pressure transmitting medium.

ORI-CHA		Ambient	0.55(1) GPa	1.05(1) GPa	1.45(1) GPa	2.10(1) GPa	2.63(1) GPa	3.04(1) GPa	3.56(1) GPa	4.31(1) GPa	5.47(1) GPa	Released
	S.G.	$R\bar{3}m$	$R\bar{3}m$	$R\bar{3}m$	$R\bar{3}m$	$R\bar{3}m$	$R\bar{3}m$	$R\bar{3}m$	$R\bar{3}m$	$R\bar{3}m$	$R\bar{3}m$	$R\bar{3}m$
	R_{wp}(%)	1.56	1.80	1.52	1.71	2.1	1.92	1.58	1.63	1.42	1.53	1.78
	χ^2	0.12	0.14	0.10	0.13	0.15	0.14	0.10	0.11	0.10	0.10	0.14
	a (Å)	9.405(5)	9.398(8)	9.386(6)	9.375(5)	9.353(3)	9.337(7)	9.332(2)	9.289(9)	9.269(1)	9.228(1)	9.406(6)
	α (°)	94.22(2)	94.13(3)	94.02(2)	93.93(3)	93.85(5)	93.83(3)	93.83(3)	93.88(1)	93.73(1)	93.76(2)	94.21(1)
	V (Å^3)	824.9(9)	823.3(3)	820.5(5)	817.8(8)	812.3(3)	808.4(4)	804.4(1)	795.7(1)	791.0(4)	780.6(3)	825.1(1)
Na-CHA		Ambient	0.51(1) GPa	1.01(1) GPa	1.55(1) GPa	2.12(1) GPa	2.52(1) GPa	3.06(1) GPa		4.06(1) GPa	5.27(1) GPa	Released
	S.G.	$R\bar{3}m$	$R\bar{3}m$	$R\bar{3}m$	$R\bar{3}m$	$R\bar{3}m$	$R\bar{3}m$	$R\bar{3}m$		$R\bar{3}m$	$R\bar{3}m$	$R\bar{3}m$
	R_{wp}(%)	1.84	1.30	1.56	1.35	2.00	1.8	1.79		1.33	1.25	1.40
	χ^2	0.16	0.10	0.10	0.10	0.15	0.12	0.12		0.10	0.10	0.10
	a (Å)	9.405(5)	9.409(1)	9.392(1)	9.385(5)	9.367(1)	9.356(1)	9.338(1)		9.298(8)	9.213(2)	9.412(2)
	α (°)	94.21(1)	94.14(1)	94.09(1)	94.17(1)	94.19(1)	94.22(1)	94.25(1)		94.32(1)	94.28(4)	94.32(1)
	V (Å^3)	824.9(9)	826.1(1)	821.8(1)	819.7(1)	814.9(1)	812.1(1)	807.2(1)		796.6(1)	775.2(4)	826.2(1)
Ag-CHA		Ambient	0.55(1) GPa	1.03(1) GPa	1.68(1) GPa	1.99(1) GPa	2.63(1) GPa	2.99(1) GPa	3.45(1) GPa	4.85(1) GPa	5.74(1) GPa	Released
	S.G.	$R\bar{3}m$	$R\bar{3}m$	$R\bar{3}m$	$R\bar{3}m$	$R\bar{3}m$	$R\bar{3}m$	$R\bar{3}m$	$R\bar{3}m$	$R\bar{3}m$	$P\bar{1}$	$R\bar{3}m$
	R_{wp}(%)	4.11	2.03	2.27	1.75	1.97	2.38	1.74	1.69	1.52	1.06	2.05
	χ^2	1.61	0.36	0.45	0.26	0.32	0.47	0.25	0.24	0.19	0.10	0.35
	a (Å)	9.421(1)	9.417(7)	9.402(2)	9.385(5)	9.38(8)	9.36(6)	9.349(9)	9.342(2)	9.332(1)	9.382(4)	9.412(2)
	b (Å)										9.112(2)	
	c (Å)										8.598(2)	
	α (°)	94.17(7)	94.21(1)	94.25(5)	94.39(9)	94.4(4)	94.4(4)	94.43(3)	94.45(5)	94.51(1)	86.29(3)	94.31(1)
	β (°)										93.00(2)	
	γ (°)										97.77(2)	
	V (Å^3)	829.2(2)	828.1(1)	823.9(1)	819.1(1)	817.6(6)	812.3(1)	809.3(1)	807.4(1)	804.6(3)	726.0(3)	826.4(1)
Li-CHA		Ambient	0.61(1) GPa	0.98(1) GPa	1.47(1) GPa	2.26(1) GPa		3.06(1) GPa		4.16(1) GPa	5.48(1) GPa	Released
	S.G.	$R\bar{3}m$	$R\bar{3}m$	$R\bar{3}m$	$R\bar{3}m$	$R\bar{3}m$		$P\bar{1}$		$P\bar{1}$	$P\bar{1}$	$R\bar{3}m$
	R_{wp}(%)	3.11	2.92	2.84	2.35	3.53		3.41		3.27	2.03	3.49
	χ^2	0.47	0.38	0.36	0.24	0.55		0.46		0.43	0.19	0.55
	a (Å)	9.396(6)	9.389(9)	9.38(8)	9.374(4)	9.359(9)		9.317(1)		9.307(3)	9.242(2)	9.399(2)
	b (Å)							9.299(2)		9.273(2)	9.319(3)	
	c (Å)							9.067(2)		8.924(2)	8.881(6)	
	α (°)	94.88(8)	94.86(6)	94.86(6)	94.75(5)	94.89(9)		91.00(3)		90.60(3)	91.79(4)	94.8(8)
	β (°)							92.48(1)		92.47(4)	92.46(5)	
	γ (°)							95.72(2)		96.53(2)	96.61(3)	
	V (Å^3)	819.9(9)	818.3(1)	815.9(1)	814.6(6)	810.2(1)		780.7(3)		764.4(2)	758.5(5)	821.1(1)
K-CHA		Ambient	0.49(1) GPa	1.00(1) GPa	1.49(1) GPa	2.13(1) GPa	2.62(1) GPa	3.00(1) GPa		4.01(1) GPa	5.12(1) GPa	Released
	S.G.	$R\bar{3}m$	$R\bar{3}m$	$R\bar{3}m$	$R\bar{3}m$	$R\bar{3}m$	$R\bar{3}m$	$R\bar{3}m$		$R\bar{3}m$	$P\bar{1}$	$R\bar{3}m$
	R_{wp}(%)	2.63	3.52	3.76	4.01	3.32	3.40	3.41		2.81	2.44	3.91
	χ^2	0.36	0.62	0.73	0.81	0.51	0.55	0.57		0.37	0.27	0.73
	a (Å)	9.43(3)	9.425(5)	9.405(5)	9.384(4)	9.363(3)	9.355(5)	9.34(4)		9.307(1)	9.285(1)	9.427(7)
	b (Å)										9.291(3)	
	c (Å)										8.816(2)	
	α (°)	94.39(9)	93.97(7)	93.85(5)	93.86(6)	93.8(8)	93.74(4)	93.71(1)		93.59(1)	90.77(3)	94.3(3)
	β (°)										93.95(2)	
	γ (°)										93.47(2)	
	V (Å^3)	830.8(8)	830.8(8)	826.1(1)	820.5(5)	815.3(1)	813.3(1)	809.4(1)		801.4(2)	757.3(2)	830.3(3)
Rb-CHA		Ambient	0.51(1) GPa	0.92(1) GPa	1.73(1) GPa	2.24(1) GPa		3.20(1) GPa	3.96(1) GPa	4.87(1) GPa	6.04(1) GPa	Released
	S.G.	$R\bar{3}m$	$R\bar{3}m$	$R\bar{3}m$	$R\bar{3}m$	$R\bar{3}m$		$R\bar{3}m$	$R\bar{3}m$	$P\bar{1}$	$P\bar{1}$	$R\bar{3}m$

	R_{wp}(%)	1.84	2.54	2.36	2.16	1.56	2.11	1.52	2.02	1.87	4.88
	χ^2	0.47	0.50	0.44	0.36	0.18	0.34	0.17	0.32	0.26	1.84
	a (Å)	9.416(6)	9.417(7)	9.406(6)	9.39(9)	9.379(9)	9.352(2)	9.35(5)	9.24(4)	9.218(2)	9.416(1)
	b (Å)								9.352(3)	9.342(4)	
	c (Å)								8.967(2)	8.933(5)	
	α (°)	94.69(9)	94.45(5)	94.42(2)	94.36(6)	94.36(6)	94.42(2)	94.56(1)	91.51(2)	91.9(9)	94.58(1)
	β (°)								92.72(2)	92.86(4)	
	γ (°)								95.01(2)	95.3(3)	
	V (Å^3)	826.0(1)	827.2(2)	824.3(3)	820.5(1)	817.5(5)	810.2(1)	809.2(3)	770.2(2)	764.5(4)	826.4(2)
Cs-CHA		Ambient	0.45(1) GPa	0.98(1) GPa		2.15(1) GPa	2.87(1) GPa		4.09(1) GPa	5.24(1) GPa	Released
	S.G.	$R\bar{3}m$	$R\bar{3}m$	$R\bar{3}m$		$R\bar{3}m$	$R\bar{3}m$		$P\bar{1}$	$P\bar{1}$	$R\bar{3}m$
	R_{wp}(%)	2.23	3.44	5.00		3.49	3.57		1.96	1.87	3.52
	χ^2	0.25	0.58	1.23		0.57	0.57		0.17	0.16	0.58
	a (Å)	9.427(7)	9.429(9)	9.415(5)		9.383(3)	9.363(3)		9.296(2)	9.269(1)	9.427(1)
	b (Å)								9.313(1)	9.261(2)	
	c (Å)								9.324(1)	9.328(1)	
	α (°)	94.25(5)	94.26(6)	94.26(6)		94.21(1)	94.22(2)		94.53(1)	94.78(1)	94.24(4)
	β (°)								95.27(1)	95.19(2)	
	γ (°)								93.5(5)	92.96(2)	
	V (Å^3)	830.4(4)	831.0(1)	827.3(3)		819.1(1)	813.7(1)		799.4(2)	793.2(2)	830.5(1)

595